

Morphological Classification of Galaxies by Shapelet Decomposition in the Sloan Digital Sky Survey II: Multiwavelength Classification

Brandon C. Kelly
Steward Observatory, Tucson, AZ 85721-0065
bkelly@as.arizona.edu

Timothy A. McKay
Physics Department, University of Michigan, Ann Arbor, MI 48109-1090
tamckay@umich.edu

ABSTRACT

We describe application of the ‘shapelet’ linear decomposition of galaxy images to multi-wavelength morphological classification using the u , g , r , i , and z -band images of ~ 1600 galaxies from the Sloan Digital Sky Survey. This combination of morphological information in a variety of bands is unique, and it allows automatic separation of different classes in ways which is impossible using single band images or simple spectroscopic measurements such as color. We utilize elliptical shapelets to remove to first-order the effect of inclination on morphology. After decomposing the galaxies we perform a principal component analysis to reduce the number of dimensions of the shapelet space to ten. We also find that each of these ten principal components contains unique spectro-morphological information, and give a description of each principal component’s contribution to a galaxy’s morphology. We find that galaxies of different broad Hubble type separate cleanly in the principal component space. In order to overcome computational limitations, we combine four of the principal components with similar morphology into two. We apply a Gaussian mixture model to this 8-dimensional space spanned by these principal components and use the results as a basis for classification. Using the mixture model, we separate galaxies into four classes and give a description of each class’s physical and morphological properties. We find that two of the mixture model classes correlate well with the traditional Hubble types, both in their morphology and their physical parameters (e.g., color, velocity dispersions, etc.). In addition, we find an additional two classes of more complex and irregular morphology that do not map well to Hubble type; most of these galaxies exhibit post-starburst activity. We compare our method to a simple cut on $u - r$ color and find the shapelet method to be superior in separating galaxies. Our framework provides an objective and quantitative alternative to traditional mono-wavelength visual classification, and the powerful use of both spectral and morphological information gives our method an advantage over separation techniques based on simpler calculations.

Subject headings: methods : data analysis — methods : statistical — techniques : image processing — galaxies : fundamental parameters — galaxies : statistics

1. INTRODUCTION

Morphological classification has remained an active and fundamental area of extragalactic as-

tronomy. Traditional classification based on the Hubble sequence (Hubble 1936) has played an important role in the development of the morphological study of galaxies. As data sets grow larger

and more precise, the Hubble scheme is becoming increasingly inadequate as a framework in which to do morphological classification (e.g, see Conselice 2003; van den Bergh, Cohen, & Crabbe 2001; Abraham et al. 1996a). Hubble based his system on the B -band morphologies of galaxies, and classification has almost exclusively relied on B -band data. Early multi-wavelength studies of galaxies include the discovery of “red arms” by Zwicky (1955) and a comparison of the disk and arm structure of six spirals by Schweizer (1976). In recent years, numerous studies have been done comparing the optical and near-infrared (near-IR) morphologies of galaxies (e.g., Colbert, Mulchaey, & Zabludoff 2001; Jarrett 2000; Block & Wainscoat 1991). Eskridge et al. (2002) have shown that, on average, galaxies with B -band classifications Sa through Scd appear about one “T-type” (de Vaucouleurs, de Vaucouleurs, & Corwin 1976) earlier in the H -band, albeit with large scatter.

Because observations in different bands probe different stellar populations, there is significant motivation for developing a multi-wavelength morphological classification system. It is well known that for the case of spiral galaxies, the shorter wavelength (e.g., the B -band) morphology is dominated by knotty regions of young stars and star-forming regions, while the longer wavelength morphology is dominated by older stars with a smoother spatial distribution. For example, Whyte et al. (2002) find that late type galaxies are more asymmetric in the B -band than in the H -band, representing the prevalence of the patchy, irregular star forming regions at shorter wavelengths. In addition, they find that galaxies are more concentrated in the IR than in the optical; however, this may be either the result of a difference in optical depth between the two bands near the center of galaxies, or because there is a greater ratio of flux farther from the center in the optical band (i.e., in the star-forming regions). Morphological classification based on images in just one observing band is unable to take advantage of variations in the overall stellar population of the galaxy (its average SED), nor of variations in the stellar population across the galaxy (color variations within the galaxy). Furthermore, differences in absorption between observing bands can result in structures being obscured by dust, sometimes leading to noticeably different morphologies

(Eskridge et al. 2002; Block & Puerari 1999).

The inherent subjectivity in the Hubble framework has motivated the development of new and quantitative morphological classification schemes. The most common of these is based on a central concentration and asymmetry measurement (Morgan 1958; Doi, Fukugita, & Okamura 1993; Abraham et al. 1996b; Conselice 2003). Recent work has investigated utilizing the Gini coefficient for quantifying morphology (Abraham, van den Bergh, & Nair 2003; Lotz, Primack, & Madau 2003). In addition, with the advent of large astronomical databases, such as the Sloan Digital Sky Survey (SDSS, York et al. 2000), manual classification is becoming extraordinarily impractical. Neural networks have proven effective at replicating the Hubble classifications of human classifiers (Odewahn 1995; Ball et al. 2003), although they have not resulted in any progress toward a new and quantitative morphological classification framework. Furthermore, many of the proposed classification schemes have only been applied to data from one observing band. A multi-wavelength quantitative classification of spiral bars was developed by Whyte et al. (2002), and both Whyte et al. (2002) and Lauger, Burgarella, & Buat (2003) have investigated the dependence of central concentration and asymmetry measurements with wavelength. In addition, Abraham, van den Bergh, & Nair (2003) and Lotz, Primack, & Madau (2003) have described the dependence of their methods on observing band. A near-IR ($2.1\mu\text{m}$) classification scheme was developed by Block & Puerari (1999) based on the pitch angle and Fourier modes of a spiral galaxy. Their classification scheme was developed for the purpose of developing a dust-penetrating morphological classification system with emphasis on the the Population II stars, and they did not find any relationship between their near-IR classes and the optical Hubble classes. While useful, non-optical classification frameworks are still based on one observing band and are incomplete in the sense that it facilitates different classifications for different parts of the spectrum; i.e., independent classification schemes are developed for the optical and near-IR morphologies.

In a previous paper (Kelly & McKay 2003, hereafter Paper I), we set forth a new classification scheme based on the shapelet (Refregier 2003) de-

composition of the r -band images of a volume-limited sample of ~ 3000 SDSS galaxies. We applied a Karhunen-Loeve (KL) transform (or principal component analysis) to the shapelet coefficients and used a mixture of Gaussians model to estimate the density of the galaxies in the space spanned by the first nine KL modes. The mixture model was used as a classification framework, where each Gaussian is identified with a morphological class. Developing a morphological classification system in this manner has the advantage of being model-independent, quantitative, and automatic. Motivated by the results of our previous analysis, and by the advantages of a multi-wavelength classification scheme, we have performed a similar analysis of SDSS galaxies using the images from all five bands: $u, g, r, i,$ and z . In addition, because we used circular shapelets in the decompositions of Paper I, the axis ratio information was found to contaminate most, if not all, of the principal components. This is obviously undesirable, as axis ratio is most strongly a result of a galaxy's orientation along our line of sight, and not of its intrinsic morphology. To remedy this, we perform our analysis in this paper with elliptical shapelets, removing, to first order, the effect of inclination on morphology.

2. SHAPELETS

Most of the shapelet formalism can be found in Refregier (2003), and Paper I describes the necessary information for our work. For completeness, we summarize a few of the important points.

Shapelets form a complete orthonormal set, and happen to be the eigenstates of the quantum harmonic oscillator Hamiltonian. The 1-dimensional basis functions are

$$B_n(x; \gamma) \equiv \gamma^{-1/2} \phi_n(x/\gamma), \quad (1)$$

where γ is a characteristic scale, n is a non-negative integer denoting the order, and the dimensionless basis functions ϕ_n are

$$\phi_n(x) \equiv \left[2^n \pi^{1/2} n! \right]^{1/2} H_n(x) e^{-x^2/2}. \quad (2)$$

Here, $H_n(x)$ is a Hermite polynomial of order n . Shapelets are orthonormal over $(-\infty, \infty)$.

The 2-dimensional shapelets are easily con-

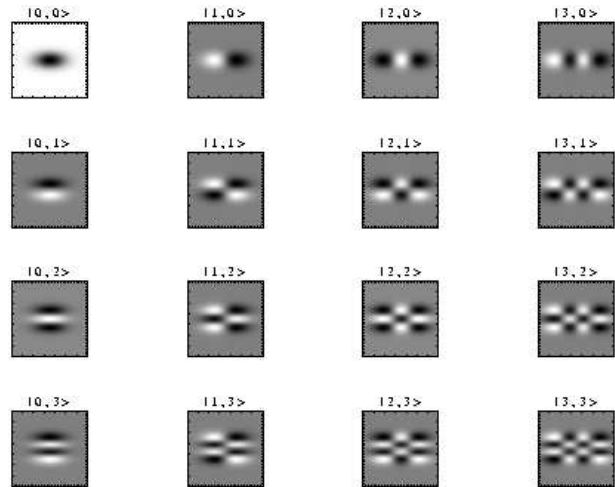


Fig. 1.— The first several elliptical shapelets.

structed from the 1-dimensional:

$$B_{n_1, n_2}(x_1/\gamma_1, x_2/\gamma_2) \equiv (\gamma_1 \gamma_2)^{-1/2} \phi_{n_1}(x_1/\gamma_1) \phi_{n_2}(x_2/\gamma_2). \quad (3)$$

Any sufficiently well behaved function (e.g., a galaxy image) can be decomposed into a sum of shapelets as

$$f(\mathbf{x}) = \sum_{n_1, n_2=0}^{\infty} f_{\mathbf{n}} B_{\mathbf{n}}(\mathbf{x}; \gamma), \quad (4)$$

with shapelet coefficients found from the orthonormality property:

$$f_{\mathbf{n}} = \int_{-\infty}^{\infty} f(\mathbf{x}) B_{\mathbf{n}}(\mathbf{x}; \gamma) d^2x. \quad (5)$$

Here, we have used the notation $\mathbf{n} = (n_1, n_2)$, $\mathbf{x} = (x_1, x_2)$, and $\gamma = (\gamma_1, \gamma_2)$. In addition, we will also use Dirac notation to denote the shapelet states, where the n^{th} state is denoted as $|n\rangle$ and has x -space representation $\langle x|n\rangle = \phi_n(x)$. Figure 1 shows the first several elliptical shapelets.

3. THE DATA

The SDSS (York et al. 2000) has been producing imaging and spectroscopic surveys of the Northern Galactic Cap over π steradians. A 2.5m telescope at the Apache Point Observatory, Sunspot, New Mexico, observes the sky in five

bands (u, g, r, i, z , Fukugita et al. 1996; Hogg, Finkbeiner, Schlegel, & Gunn 2001; Smith et al. 2002) between 3000 and 10000 Å, using a drift-scanning mosaic CCD camera (Gunn 1998), which detects objects to a flux limit of $r \sim 22.5$ mags. The survey, when finished, is expected to spectroscopically observe 900,000 galaxies down to $r_{lim} \approx 17.77$ mags (Strauss et al. 2002), 100,000 Luminous Red Galaxies (Eisenstein 2001), and 100,000 quasars (Richards 2002). The spectroscopic follow-up uses two digital spectrographs on the same telescope as the imaging camera, and the spectroscopic samples are assigned plates and fibers using an algorithm described by Blanton et al. (2003). The astrometric calibration is described in Pier et al. (2003). Details of the galaxy survey can be found in the galaxy target selection paper (Strauss et al. 2002), and other principles of the survey are described in the Early Data Release (Stoughton et al. 2002, EDR,). Details of the First Data Release (DR1) can be found in Abazajian et al. (2003)

As in Paper I, we use two samples in this analysis. We first investigate the shapelet method using the u, g, r, i , and z -band data for 184 of the 1482 well-resolved galaxies used by Nakamura et al. (2003, hereafter Sample 1) to estimate the morphology-dependent luminosity function. We have chosen this group in order to compare the shapelet results with traditional Hubble type, as this catalog contains manual classifications of Hubble type. The manual classifications make no distinction between spirals with bar structure and spirals without. Sample 1 contains those galaxies of the Nakamura et al. (2003) sample that have redshifts $z < 0.07$ and a PSF width of less than 2.0 kpc when projected onto the plane of the galaxy in all five bands. This allows us to smooth all galaxies of Sample 1 to a constant scale before decomposing them (see § 4). These galaxies are included in the SDSS EDR.

We next investigate the shapelet method on the images from all five bands of a volume-limited sample of 1579 nearby galaxies (hereafter Sample 2) included in the SDSS DR1. These galaxies were chosen because they have projected PSF widths of less than our desired resolution of 2.0 kpc, allowing us to smooth them to this scale in all five bands. They have redshifts $z < 0.07$ and absolute magnitudes $U \leq -16, G \leq -18$ and $R, I, Z \leq -19$. We

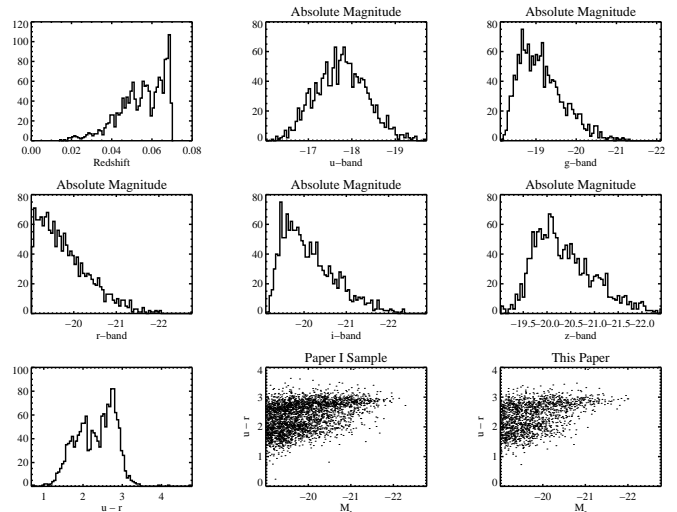


Fig. 2.— The distributions of redshift, absolute magnitude, and $u - r$ color for the galaxies of Sample 2. Note that there are no systematic differences between the sample of galaxies used in Paper I and that used in this analysis.

made the redshift cut at $z = 0.07$ because projected PSF widths become larger than 2.0 kpc for redshifts greater than this, and we chose galaxies of these absolute magnitudes to allow a uniform distribution of absolute magnitude with redshift. Although we started with the same galaxies as in Paper I, we were left with only ~ 1600 galaxies after making these same cuts on all five bands, as opposed to ~ 3000 after making the cuts on only the r -band data. In addition, we omitted galaxies for which necessary information was missing or had large errors in their shapelet reconstruction in at least one of the five bands. Figure 2 displays the redshift, absolute magnitudes, and $u - r$ color distributions for this sample.

4. DECOMPOSITION METHOD

Most of the information regarding our decomposition method can be found in Paper I; here we reiterate the important points as well as the additions to the method introduced as a result of including images at different wavelengths and using elliptical shapelets. We calculate the position angle of the galaxy, θ_{pos} , from the r -band data and rotate the image for each band by θ_{pos} . This

assures that all galaxies are oriented with their r -band major axis oriented along the horizontal.

In Paper I, we used shapelets characterized by a single scale, γ . While the use of circular shapelets includes the necessary morphological information for classification, information regarding the galaxy’s axis ratio contaminates the principal components and the resulting classification scheme. To remedy this problem, we use shapelets of varying ellipticity, where the scales along the major and minor axis are γ_1 and γ_2 , respectively. The axis ratio of the shapelets is then $b/a = \gamma_2/\gamma_1$. The shapelet scales, γ_1 and γ_2 , are calculated as

$$\begin{aligned}\gamma_1 &= \left[\frac{I_{xx} + I_{yy}}{1 + (b/a)^2} \right]^{1/2} \\ \gamma_2 &= \left(\frac{b}{a} \right) \gamma_1,\end{aligned}\quad (6)$$

where I_{xx}, I_{yy} are the r -band adaptively weighted moments (Fischer et al. 2000) in the horizontal and vertical directions, and b/a is the r -band axis ratio of the galaxy. If $\gamma_i < \beta$, where β is the largest PSF scale in all bands, then $\gamma_i = \beta$. If necessary, we pad the image with blank sky out to a distance $10\gamma_i$ and use the value of σ_{sky} for that band to add artificial noise. This assures the orthogonality of the shapelets. The mean of the image is subtracted before decomposition.

As outlined in Paper I, we desire to have all galaxies resolved on the same physical scale, ensuring that differences in shapelet coefficients are not the result of differences in resolution. To do this, we artificially redshift the galaxies to $z = 0.07$, which defines the upper limit of our sample. We then smooth the galaxies in each band by a Gaussian of standard deviation $\beta' = \sqrt{\beta_0^2 - \beta^2}$, where β_0 is the scale of the PSF that would resolve a galaxy on the chosen standard physical scale. The new shapelet scales, γ'_i , become $\gamma'_i = \sqrt{\gamma_i^2 + \beta'^2}$. We use γ'_i to correct for the loss of resolution resulting from the additional smoothing, ensuring that $\gamma'_i \geq \beta_0$.

We then calculate the shapelet coefficients by decomposing the galaxy image about its center in each band up to a maximum order of $n_{max} = n_1 + n_2$. We compute the center of the image from the shapelet coefficients (see Paper I) and decompose the galaxy about this new center. We iterate this procedure twice. We calculate the flux of

the image in each band from the shapelet coefficients, and divide the shapelet coefficients by the total combined flux. This keeps information regarding the differences in a galaxy’s flux between bands and ensures that galaxies of different total luminosities do not have different shapelet coefficients; i.e., only information regarding a galaxy’s morphology and its flux ratios between the bands u, g, r, i , and z are included in the shapelet coefficients.

As with Paper I, we choose to decompose the galaxies up to a maximum order of $n_{max} = 12$, and use a standard physical width of $\beta_0 = 2.0$ kpc. Figure 3 shows the images of four Hubble-classified galaxies in each band before and after artificial redshifting and smoothing, and Figure 4 shows a galaxy reconstructed from its shapelet coefficients.

5. PRINCIPAL COMPONENT ANALYSIS

5.1. The Transform

In order to reduce the dimensionality of our data set, we perform a principal component analysis (KL-transform) on the shapelet coefficients for the galaxies of Sample 2. Doing so allows us to reduce the 455-dimensional space spanned by the shapelet coefficients (91 coefficients for each band) to one that is much more manageable. Similar to the results from Paper 1, which applied the KL-transform to just the r -band images, the first few principal components contain the vast majority of the variance. The first KL-morphology contains 96.8% of the variance, and the first three contain 97.9%. We denote the j^{th} principal component as p_j and its corresponding coefficient as a_j . Further information regarding the principal component analysis can be found in Paper I.

After applying the KL-transform on the Sample 2 data, we calculate the projections of the galaxies of Sample 1 along the principal components. Doing so allows us to develop an idea of the location of the different Hubble types in the KL-space. We divide the Sample 1 galaxies into four types: early, middle, late, and edge-on. The early types include those classified by Nakamura et al. (2003) as Hubble types E–Sa, the middle types as Sab–Sbc, and the late types as Sc–Im. The edge-on class consists of middle and late type galaxies with axis ratios $b/a < 0.4$. Figure 5 shows the locations of

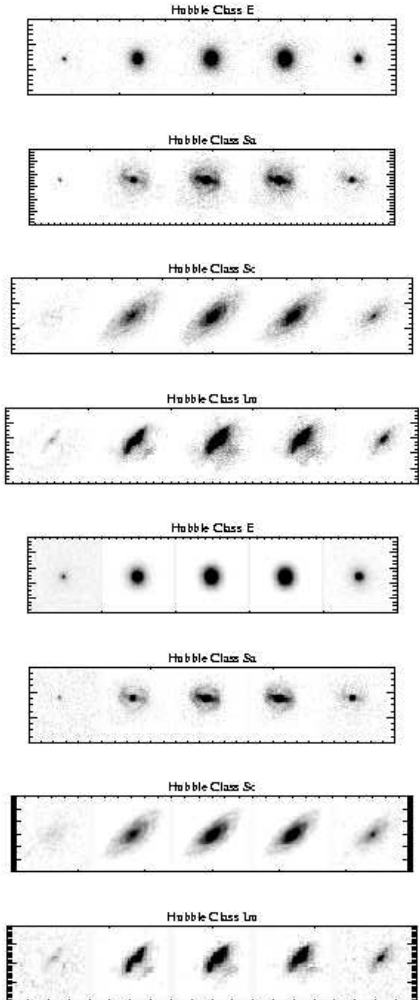


Fig. 3.— Selected galaxies from Sample 1, shown before artificial redshifting and smoothing (top) and after (bottom). For each galaxy, the images are shown in the order of u -band (left), g , r , i , and z -band (right).

the galaxies in the 2-dimensional slice spanned by p_1 and p_2 , and Figure 6 shows the a_j of the Sample 1 galaxies, divided according to Hubble type. Figure 7 shows the KL-morphologies we used for classification, constructed from their shapelet coefficients. In Table 1 we show the ratios of the absolute flux of the p_j in each band, where the absolute flux is the sum of the absolute values of the pixels that make up the constructed principal component image.

5.2. Description of the Principal Components

The first principal component is very similar to p_1 found from using just the r -band images in Paper I. It has an exponential profile in all five bands and its morphology does not change between the different bands. The vast majority of the variance is contained within p_1 , and, as a result, its coefficients, a_1 , are significantly higher than the other a_j . This implies that p_1 may be interpreted as the basic galaxy morphology, where further and comparatively small modifications introduced from the other p_j serve to form a galaxy’s unique shape. In other words, galaxies appear to be constructed starting with a p_1 -like component, which is then modified with additional components. Furthermore, p_1 does not contain any holes of negative flux, nor are any of the coefficients negative, as would be expected if p_1 forms the ‘basic’ galaxy morphology. The flux ratios for p_1 are consistent with the average flux ratios of typical galaxies. In addition, as can be seen from Figure 6, the Hubble types separate very well along p_1 , with the late types having the smallest values of a_1 and the early types having the largest.

In Figures 8 and 9 we show the dependence of the r -band concentration index, C , and $u-r$ color as a function of the a_j . The concentration index is a common morphological measurement which we define the same way as in Paper I:

$$C = 5.0 \log_{10} \left(\frac{r_{90}}{r_{50}} \right). \quad (7)$$

Here, r_{90} and r_{50} are the radii where the Petrosian ratio, η , is equal to 0.1 and 0.5, respectively. More concentrated galaxies (e.g., early types) will have higher values of C . As can be seen, the concentration index has some correlation with a_1 , where more concentrated galaxies have higher values of

TABLE 1
FLUX RATIOS OF THE KL-MORPHOLOGIES.

KL-mode	u	g	r	i	z
PC 1	0.022	0.210	0.325	0.348	0.095
PC 2	0.081	0.331	-0.200	-0.273	-0.115
PC 3	0.026	0.216	0.320	0.341	0.097
PC 4	-0.025	-0.156	-0.355	-0.388	0.079
PC 5	0.027	0.212	0.326	0.355	0.081
PC 6	0.027	0.167	0.282	0.314	0.210
PC 7	0.034	-0.159	-0.230	-0.296	0.282
PC 8	-0.026	-0.226	-0.311	-0.339	-0.097
PC 9	-0.032	-0.232	-0.287	-0.370	-0.079
PC 10	0.034	0.222	0.287	0.387	-0.070

NOTE.—Flux ratios are calculated by summing over the absolute value of the pixels in the p_j images in each band, divided by the total for all bands. A negative value denotes that the total flux is negative for that band.

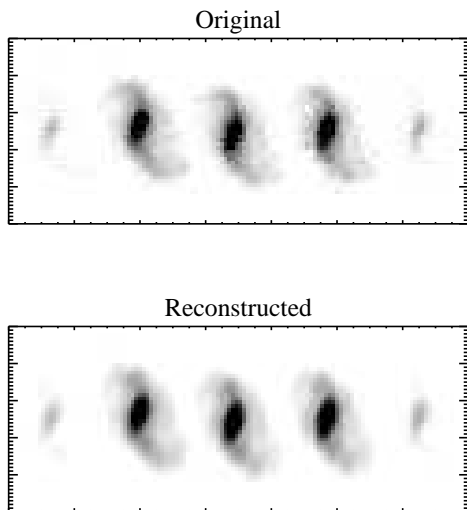


Fig. 4.— Original Image of a galaxy and the galaxy image reconstructed from its elliptical shapelet coefficients for $n_{max} = 12$.

a_1 . We interpret this as representing the fact that more concentrated galaxies have morphologies most similar to that of p_1 , so fewer modifications are needed. This results in a larger value of a_1 , or rather smaller values of the coefficients of the other principal components, decreasing their relative contributions to the final morphology. In addition, there is structure in the space spanned by $u - r$ and a_1 , although there is does not appear to be any correlation. This structure is very similar to that seen in the space spanned by a_1 and a_2 . This is expected, given the strong anticorrelation between a_2 and $u - r$.

The second principal component includes a significant amount of the broad-band color information. It has the most absolute flux in the g -band, and is ‘blue’ in the sense that the flux is positive for the u and g bands and negative for the redder bands. In addition, p_2 contains a much greater fraction of u and g -band flux than the other p_j . The flux in the central region becomes progressively lower until it becomes negative in the r -band image and continues on to more negative values in the i and z -bands. The spectral contribution from p_2 to p_1 is the most significant of the p_j , in the sense that the addition of p_2 to p_1 changes the flux ratios between the bands more than any other p_j . The values of a_2 are highly anticorrelated with $u - r$ color, as can be seen from Figure 9. It is interesting to note that the zero point of a_2 occurs at a value of $u - r \sim 2.3$. This is very close to the optimal color separator ($u - r = 2.22$) of the bi-

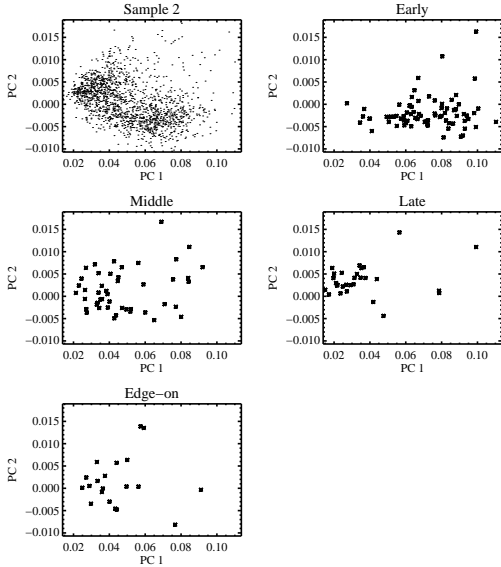


Fig. 5.— Locations of the galaxies of Sample 2 (top left plot) and Sample 1 in the 2-dimensional slice spanned by p_1 and p_2 . Using the reference galaxies from Sample 1, we are able to see that the different Hubble types are well separated in this plane.

modal distribution of galaxies in color space found from SDSS data (Strateva et al. 2001; Baldry et al. 2003). Late types have positive values of a_2 , while the early types have negative values, as would be expected from the well known color-morphology relationship. Morphologically, positive values of a_2 have the effect of decreasing the flux near the edge of the galaxy, reducing its size. Negative values do the opposite, increasing the size; this tends to make galaxies more extended. In addition, we note that a_2 is also correlated with concentration index, however this is just a reflection of the fact that concentration index is correlated with $u - r$, and a_2 is highly correlated with $u - r$.

The third, fifth, and eighth KL-morphology, p_3 , p_5 , and p_8 , are similar to p_2 in the sense that the negative flux becomes progressively more dominant at longer wavelengths. The flux ratios of these p_j are nearly the same as those of p_1 . These principal components contain an area of concentrated positive flux near the center, surrounded by a ring of negative flux. The relative size of

the area of positive flux to the ring decreases at higher wavelengths. Positive values of a_3 , a_5 , and a_8 result in making the galaxy bluer and decreasing the ratio of the ‘bulge’ to the ‘disk’, as well as making an important contribution to defining the bulge and disk. Negative values broaden the size of the central bulge as well as the outer low surface brightness ‘envelope’, giving the galaxy a more early type morphology. These three principal components also contain some information regarding asymmetry along the minor axis. The most notable differences between these p_j is in the z -band morphology and the fact that the sharp central region of positive flux is slightly offset from the center in the vertical direction for p_3 and p_5 . There does not appear to be any separation of Hubble type along these p_j . Oddly, p_3 , p_5 , and p_8 are not correlated with concentration index. This may be due to the fact that the concentration index, as it is defined in this work, is merely dependent on the ratio between r_{90} and r_{50} . While these p_j may serve to narrow or broaden the galaxy radial profile, their addition may not necessarily change the ratio of r_{90} to r_{50} .

The fourth principal component, p_4 , is asymmetric about the major axis. The basic morphology remains constant throughout the different bands, however the area of positive flux in the g -band is noticeably smaller than that seen in the other bands. As is usual, the u -band morphology is more irregular and patchy than the others. The flux for this KL-mode is mostly in the r and i bands. The contribution from p_4 is predominately morphological, as the addition of p_4 to p_1 has almost no effect on the flux ratios. This p_j is similar to the sixth principal component derived from just the r -band images in Paper I; it may be thought of as a weighted asymmetry measurement where asymmetry near the center is given the most weight. There does not appear to be any correlation between p_4 and C or $u - r$.

The sixth and seventh principal components have similar morphologies, but opposite g , r , and i flux values. They have a much larger fraction of their total absolute flux in the z band than the other p_j . Their u and z -band morphologies are relatively simple regions of positive flux, while their g , r , and i -band morphologies consist of alternating ‘bumps’ of positive and negative flux along the major axis. Late Hubble types appear to have an

almost symmetric distribution of a_6 about zero, early types are more likely to have positive a_6 , and the middle and edge-on types have mostly negative a_6 . For p_7 , the early types have mainly negative a_7 , while the distribution of the others peaks at zero and is extended in the positive direction. Positive values of a_6 (and negative values of a_7) widen the light profile along the major axis, increasing the size of the central high surface brightness region (i.e., the ‘bulge’) relative to the extended outer low surface brightness region. Negative a_6 (positive a_7) have the opposite effect, making the separation between a bulge and disk component noticeable. In addition, p_6 and p_7 cause a small change in the flux distribution across the bands. These principal components are uncorrelated with concentration index, however there does appear to be structure in the space spanned by these a_j and $u - r$ similar to that seen with a_1 . The coefficients of p_6 and p_7 are the only a_j that appeared to exhibit any correlation with axis ratio, b/a , although even in this case the correlation is minimal. This is encouraging, as it reinforces the fact that using elliptical shapelets nearly nullifies any contribution to the a_j that results from differences in inclination.

The ninth and tenth principal components have a high surface brightness central region that is twisted with respect to the low surface brightness ‘envelope’ in all of the bands except for u , where the morphology is more irregular and asymmetric. This results in a morphology where a galaxy’s inner isophotes are twisted relative to the outer isophotes. Similar to p_6 and p_7 , p_9 and p_{10} are opposite in orientation and in the sign of their flux. The twisting induced by p_9 and p_{10} is most pronounced in the i -band morphology. As would be expected, the Hubble types do not separate along p_9 .

We use the 8-dimensional space spanned by $\{p_1, p_2, p_3, p_5, p_4, p_{6-7}, p_8, p_{9+10}\}$ to do the mixture model classification (see § 6). Here, $p_{6-7} = (p_6 - p_7)/\sqrt{2}$ and $p_{9+10} = (p_9 + p_{10})/\sqrt{2}$. Ideally, we would like to perform the classification on the 10-dimensional space spanned by the first ten principal components, however because of computational limitations it becomes difficult to perform the mixture model classification on the sample used here for more than eight dimensions. For this reason, we combine the values for p_6 and p_7 ,

as well as p_9 and p_{10} . We choose to combine these four p_j because they appeared to exhibit the most similarity; p_6 is very similar to $-p_7$, and p_9 is very similar to $-p_{10}$ rotated clockwise by $\pi/2$. We use $p_6 - p_7$ as opposed to $p_6 + p_7$ because of the asymmetries in their morphologies.

6. CLASSIFICATION

We use the publicly available **fastmix** software (Moore 1999) to fit the data in the 8-dimensional space spanned by the principal components described in § 5.2 with a mixture of Gaussians model. In this model, the density of galaxies in this eight-dimensional space is fit to a mixture of eight-dimensional Gaussians. Each of these Gaussians then corresponds to a different class. We find that the distribution is best fit with four Gaussians. Paper I describes in detail our procedure for using a mixture of Gaussians model; here we present only a description of the results. We will use the notation M_k to denote the k^{th} mixture class. Figure 10 shows the locations of the galaxies in each M_k in the 2-dimensional space spanned by p_1 and p_2 in the same manner as for the Hubble types in Figure 5, and Figure 11 shows the mean a_j and standard deviation for each M_k . For the purpose of plotting, galaxies are shown as occupying the class of highest probability; however, it should be noted that because this classification scheme is continuous, each galaxy has a probability of occupying each class. In addition, Figure 12 compares the mixture classes with Hubble type, Figure 13 shows the mean morphology of each mixture class, and Figure 14 shows a representative galaxy from each M_k . Figure 15 compares some physical parameters with mixture class.

The first mixture class, M_1 , is dominated by ellipticals and some early spirals. The average Hubble type for M_1 is S0. Values of the a_j are consistent with this description: high a_1 , negative a_2 , and positive a_{6-7} . As noted above, negative values of a_2 correspond to a redder SED, and positive values of a_6 combined with negative values of a_7 create a radial profile more consistent with elliptical morphologies. The other a_j have a mean of zero for M_1 . The average physical properties of M_1 are also consistent with what is known of early type galaxies. Galaxies of M_1 have the highest velocity dispersions, are the brightest in the

r -band, have physically (kpc) small scales γ_1, γ_2 , and are the most concentrated. Spectroscopically, they are the reddest (high $u-r$) and the only class with negative mean spectral eigenclass. The SDSS spectral eigenclass (Yip et al. 2003) is a spectral classification based on a principal component analysis of 170,000 Sloan galaxies. Negative values correspond to ‘red’ ($u-r \gtrsim 2.2$) galaxies, positive values correspond to ‘blue’ galaxies ($u-r \lesssim 2.2$).

The second mixture class, M_2 , has a mean Hubble type of Sab, but with a very large spread such that one is unable to associate M_2 with any particular Hubble type. Indeed, it is almost equally populated by ellipticals and spirals. The second mixture class consist mostly of galaxies that are outliers in the KL-space, and, with the exception of p_2, p_5 , and p_8 , the average a_j for M_2 is similar to that of M_1 . Despite these similarities in the mean a_j , the width in the distribution of a_j for M_2 is significantly larger than that of any other mixture class. The difference seen in a_2 between M_1 and M_2 is because of the predominantly spectroscopic contribution of a_2 ; the non-zero averages for a_5 and a_8 may be due to a morphological correction to that of a_2 . Galaxies in M_2 display the largest amount of asymmetry in their morphologies, as can be inferred from their large $|a_4|$. Based on their spectral eigenclass, a_2 , and $u-r$ color, one can see that galaxies of M_2 cannot be classified as red or blue, as their mean values fall near the dividing line for these parameters with a very large spread. Physically, galaxies of M_2 typically have higher velocity dispersions, are the dimmest of the mixture classes, physically small, concentrated, and have the brightest half-light surface brightness, μ_{50} , in the u -band. In addition, most galaxies of M_2 (and M_4) have negative second and third spectral eigencoefficients, where the eigencoefficients are found from the same analysis as the spectral eigenclass. Galaxies with negative second and third spectral eigencoefficients exhibit post-starburst activity in their spectra (Yip et al. 2003).

The third mixture class, M_3 , is populated by normal spiral galaxies, with a mean Hubble type of Sc. This mixture class has the lowest values of a_1 , allowing the relative contributions from the other principal components to be stronger, resulting in a more complex morphology. Mixture class M_3 also has the highest mean value of a_2 , meaning that M_3 is the ‘bluest’ class. Galaxies of M_3 have neg-

ative a_{6-7} and positive a_8 , implying radial structure resembling bulge and disk components. The other a_j are on average zero. The physical parameters of this class are what would be expected for spirals: they are on average bluest, least concentrated, physically largest, and have the smallest velocity dispersions. In addition, we note that the trend seen in axis ratio with M_k is artificial; the numbering of mixture classes is arbitrary and the trend only exists because those M_k with more spirals will have a lower average axis ratio due to the fact that spirals experience a larger range in b/a than do ellipticals.

The fourth mixture class, M_4 , is also mostly populated by spirals, with a mean Hubble type of Sb. Morphologically, M_4 is on average very similar to M_3 , and in fact, only differs in its mean a_j from M_3 for p_1 and p_2 . However, despite the fact that the mean a_j are typically almost identical, these two classes differ notably in the width of their morphological distributions; M_4 always has a much larger spread in its a_j . This implies that galaxies of M_4 typically display more complex and assymetric structure than those of M_3 . Although the spread is large, galaxies of M_4 are typically redder, physically smaller, and more concentrated than those of M_3 , but more similar to M_3 in these properties than to M_1 or M_2 . Galaxies of M_4 have significantly higher velocity dispersions than those of M_3 , and in fact, the velocity dispersions of M_4 are similar to those of M_1 and M_2 . We also note that in addition to M_2 , galaxies of M_4 also display post-starburst activity in their spectra, as inferred from their second and third spectral eigencoefficients. Because M_2 and M_4 consists of galaxies with more irregular and complex morphologies, one can immediately infer that galaxies with more irregular morphologies typically display post-starburst activity in their spectra. This is interesting because these two classes are not the bluest, although show the largest spread in their $u-r$ color and spectral eigenclass.

It is interesting to compare our classifications with the simple separation of ‘red’ and ‘blue’ galaxies typically done on SDSS data with a cut on $u-r$. We show in Figure 16 a galaxy from classes M_1 and M_3 with a value of $u-r$ color unexpected for that class; e.g., because M_1 would be considered a red class ($\langle u-r \rangle > 2.22$), we show a galaxy from M_1 with $u-r$ on the blue side of the

optimal color separator ($u - r = 2.22$). In addition, to facilitate further discussion of the nature of mixture classes M_2 and M_4 , which show an almost uniform distribution in $u - r$ color, we show a very blue galaxy and a very red galaxy from both M_2 and M_4 . Many of the galaxies for M_1 and M_3 with uncharacteristic $u - r$ values for their respective class had probabilities of being in that class of $\lesssim 0.9$, implying that these galaxies have properties characteristic of more than one class. Each of the galaxies we show in Figure 16 has a probability of being in their class ≥ 0.9 .

From the images shown in Figure 16, we can see that our classification scheme is able to group galaxies of similar morphology into different classes even when such galaxies exhibit broadband color more characteristic of another class. For example, the edge-on spiral of M_4 , and to a lesser extent the face-on spiral of M_3 , is very red and has a value of $u - r$ that would be expected for ellipticals, however the mixture classification is able to effectively place these galaxies in their appropriate spectro-morphological class. Also, the galaxy of M_1 has a $u - r$ color more characteristic of spirals, however this galaxy is obviously an elliptical.

The red galaxy of M_2 has $u - r$ color characteristic of ellipticals, and the morphology of this galaxy certainly looks elliptical. However, this galaxy has a more negative value of a_8 than is characteristic for M_1 , as well as a value of a_{9+10} that is extremely negative, implying some sort of inner ‘twisting’ structure (see § 5.2) for this galaxy. The blue galaxy of M_2 is classified as M_2 for the obvious reason that it would have very large a_2 , but also because the galaxy has an asymmetric and disturbed morphology. In particular, notice the structure in the upper-right of this galaxy. Both galaxies have more irregular morphologies than would be expected for M_1 , explaining their M_2 classification.

The blue galaxy of M_4 appears to exhibit a very diffuse morphology. It is classified as M_4 (as opposed to M_3) because of its large $|a_4|$, a_5 , a_8 , and very large $|a_{9+10}|$, implying a more irregular and complex morphology than is characteristic for M_3 . The red galaxy of M_4 is an edge-on spiral and is not classified as M_3 because of its negative (red) value for a_2 .

7. CONCLUSIONS

An important project of modern extragalactic astronomy is the pursuit of a quantitative and automatic morphological galaxy classification scheme that incorporates spectroscopic information. Traditional classification is becoming more inadequate, and new systems are needed. A quantitative and multiwavelength description of morphology will allow astronomers to give quantitative relations between a galaxy’s spectral morphology and its physical parameters. In addition, automating the classification scheme allows the full use of large astronomical databases for analyzing galaxy morphology, which will be of great benefit in investigating the physical significance of a galaxy’s shape.

In this paper, we have tested the shapelet decomposition method as a quantitative and automatic description of galaxy morphology across the optical spectrum. We apply the method to a sample of ~ 1600 galaxies from the Sloan Digital Sky Survey, using the images in all five observing bands ($u, g, r, i,$ and z), and show that galaxies of known broad Hubble type separate cleanly in shapelet space. In addition, using the vast amount of SDSS data allows the admission of powerful statistical methods of analysis, such as principal component analysis and the mixture of Gaussians model. Applying the principal component analysis, we utilize the first ten eigenshapes and combine four of them into two, allowing us to work within an 8-dimensional space spanned by these morphologies. Using shapelets of ellipticity equal to that of the decomposed galaxy resulted in minimal contamination of axis ratio information in the principal components. We show that each principal component contains unique morphological information that often varies with observing band, and sufficiently separates galaxies that are known to have different morphologies.

Furthermore, we apply a mixture of Gaussians model to describe the density of galaxies in the space spanned by the principal components, where each Gaussian represents a morphological class. The mixture model fit the distribution to four Gaussians, implying four classes. The two ‘main’ classes were shown to correlate well with a broad description of Hubble type, whereas the other two classes were populated by galaxies that were often

outliers in the KL-space and could not be associated with any particular Hubble type. In addition, we show that galaxies of different morphologies differ, on average, in their physical properties. We compared our method with a simple cut on color and show that our method is superior for separating galaxies of different spectro-morphological properties. Our method is model-independent, objective, and automatic; the fact that the method is able to separate galaxies of different morphology and color so well is promising and attests to its efficacy.

8. ACKNOWLEDGMENTS

This work was supported by National Science Foundation grants AST-F007182 and AST-0206277. We would like to thank Alexandre Reffregier for the use of his shapelet code, and Erin Sheldon and Ben Koester for helping with computer issues.

Funding for the creation and distribution of the SDSS Archive has been provided by the Alfred P. Sloan Foundation, the Participating Institutions, the National Aeronautics and Space Administration, the National Science Foundation, the U.S. Department of Energy, the Japanese Monbukagakusho, and the Max Planck Society. The SDSS Web site is <http://www.sdss.org/>.

The SDSS is managed by the Astrophysical Research Consortium (ARC) for the Participating Institutions. The Participating Institutions are The University of Chicago, Fermilab, the Institute for Advanced Study, the Japan Participation Group, The Johns Hopkins University, Los Alamos National Laboratory, the Max-Planck-Institute for Astronomy (MPIA), the Max-Planck-Institute for Astrophysics (MPA), New Mexico State University, University of Pittsburgh, Princeton University, the United States Naval Observatory, and the University of Washington.

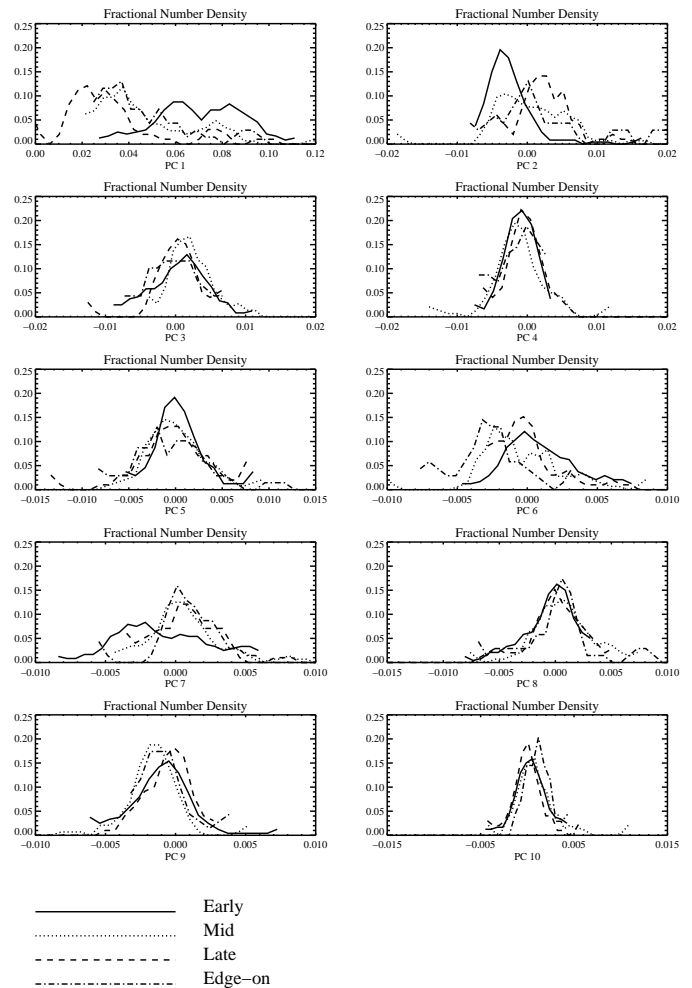


Fig. 6.— Projections of the galaxies of Sample 1 along the ten principal components used as a basis for classification. From these plots, one can see that the Hubble types are well separated along a few of the p_j .

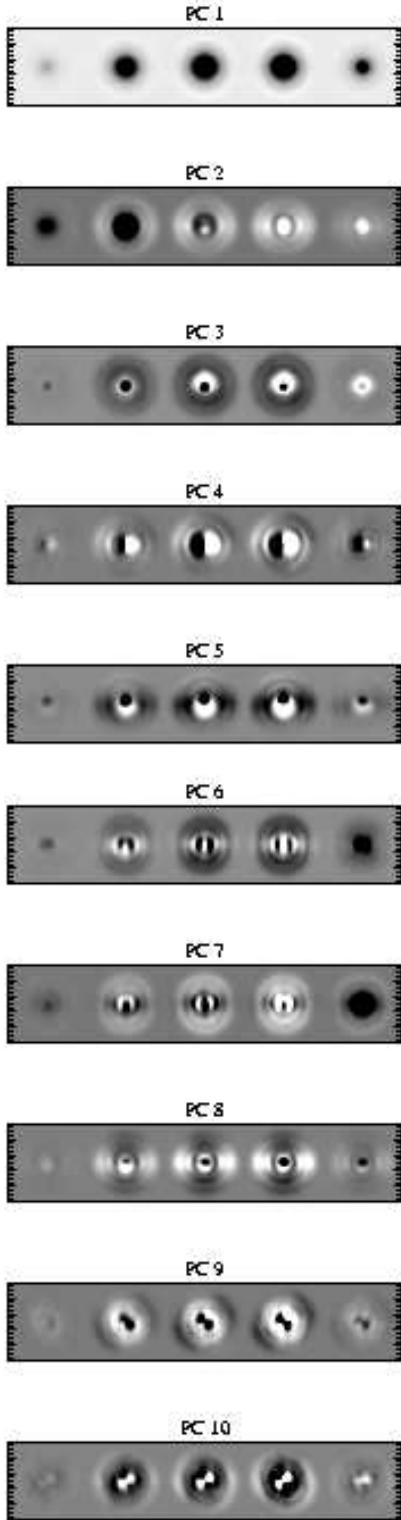


Fig. 7.— Images of the ten principal components used, constructed from their shapelet coefficients. As before, the bands of the images are (starting from the left): $u, g, r, i,$ and z .

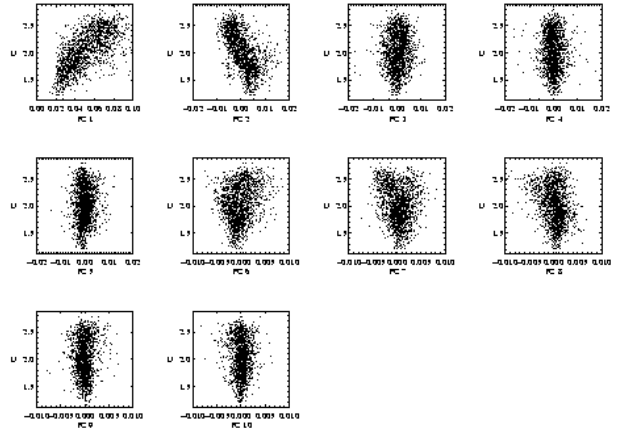


Fig. 8.— r -band concentration index as a function of the coefficients of the principal components.

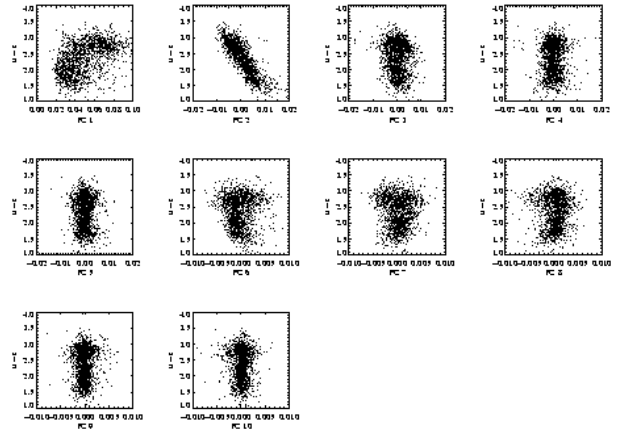


Fig. 9.— $u-r$ color as a function of the coefficients of the principal components.

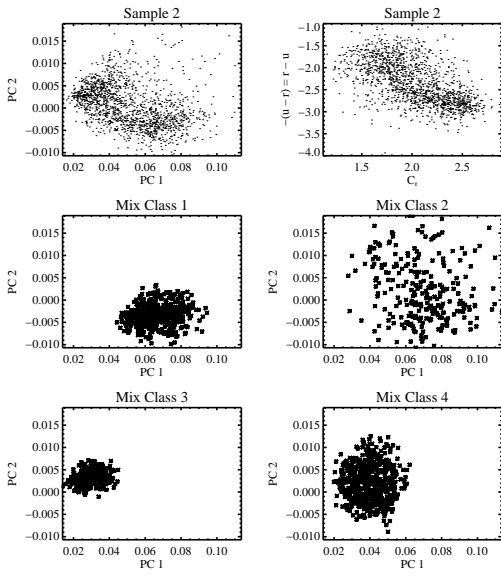


Fig. 10.— Locations of the galaxies of Sample 2 in the 2-dimensional slice spanned by p_1 and p_2 , seperated by mixture class. We show a plot of $-(u-r)$ against r -band concentration index for comparison, as C_r was shown to be have some correlation with p_1 and $u-r$ is anticorrelated with p_2 .

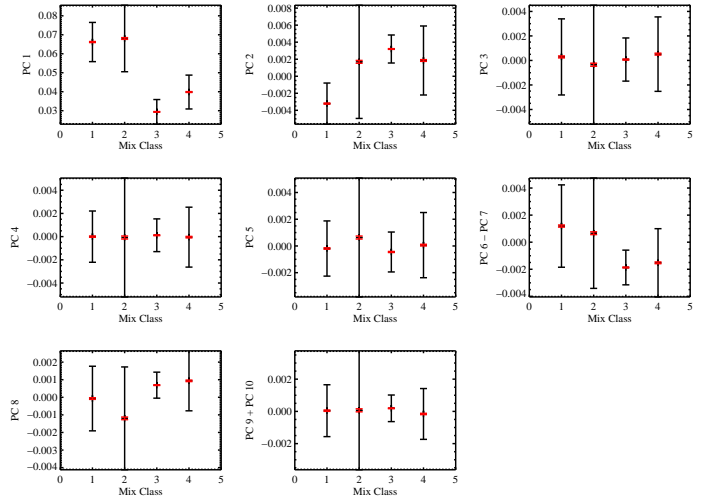


Fig. 11.— Projections along the principal components for the galaxies of Sample 2, classified by mixture model class M_k . The larger error bars show the standard deviation in the distributions, and the shorter ones show the uncertainty in the mean.

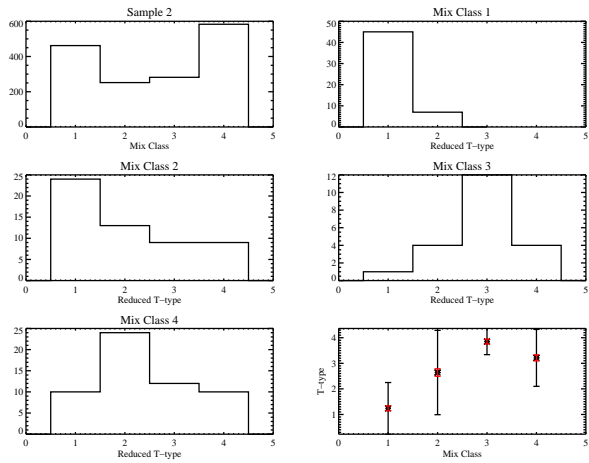


Fig. 12.— Plots comparing the results of the mixture model classification to Hubble type. The first plot (top left) shows the distribution of mixture classes for the galaxies of Sample 2. The “Reduced T-type” seen in the following histograms are based on the Hubble classifications of Sample 1 and stands for the following: 1=Early, 2=Middle, 3=Late, 4=Edge-on. The T-type values of the bottom right plot are also from the Sample 1 data, and are as follows: 0=E, 1=S0, 2=Sa, 3=Sb, 4=Sc, 5=Sdm, 6=Im. As can be seen, the Hubble types map rather well to a few of the mixture classes. The larger error bars seen in the bottom plot show the standard deviation in the distributions, and the shorter ones show the uncertainty in the mean.

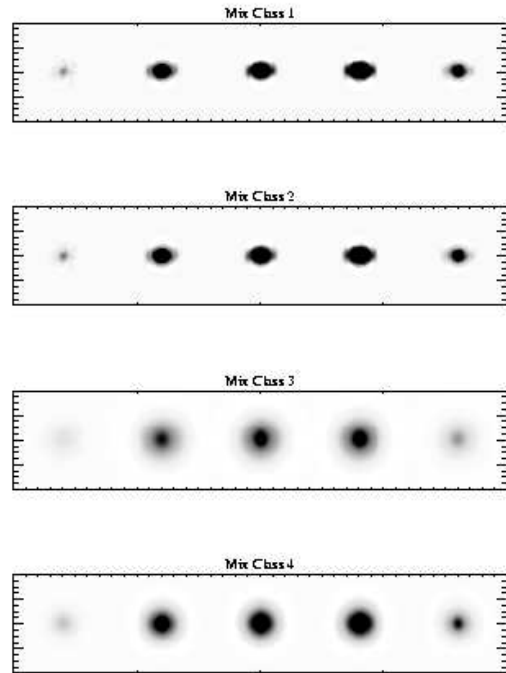


Fig. 13.— The mean morphologies of the mixture model classes, reconstructed from the mean shapelet coefficients for each respective class. As before, the bands of the images are (starting from the left): u , g , r , i , and z .

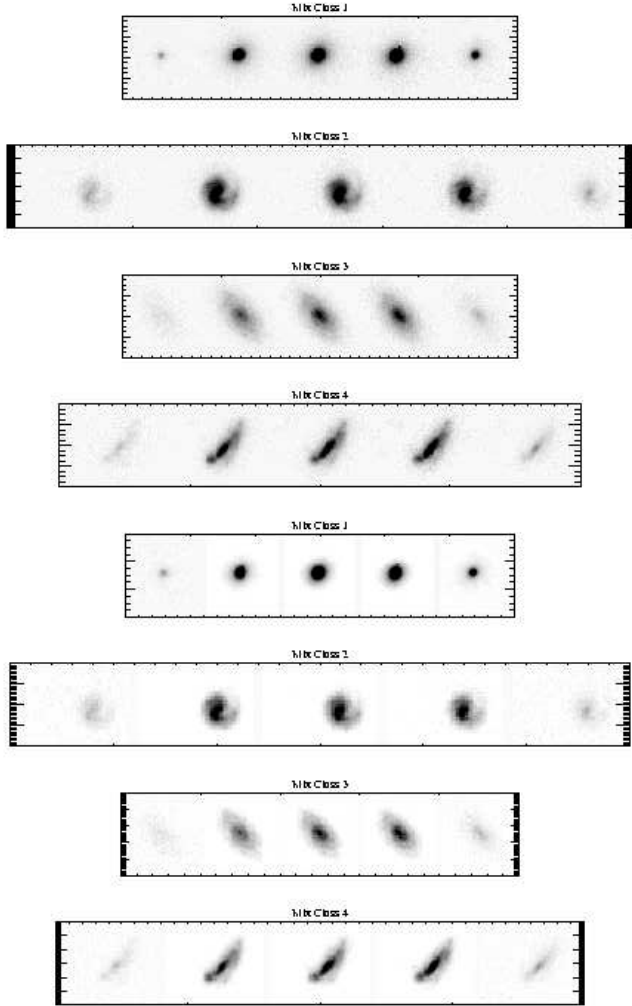


Fig. 14.— Galaxies from each M_k , shown before artificial redshifting and smoothing to a PSF width of $\beta_0 = 2.0$ kpc (top) and after (bottom). The bands of the images are (starting from the left): u, g, r, i , and z .

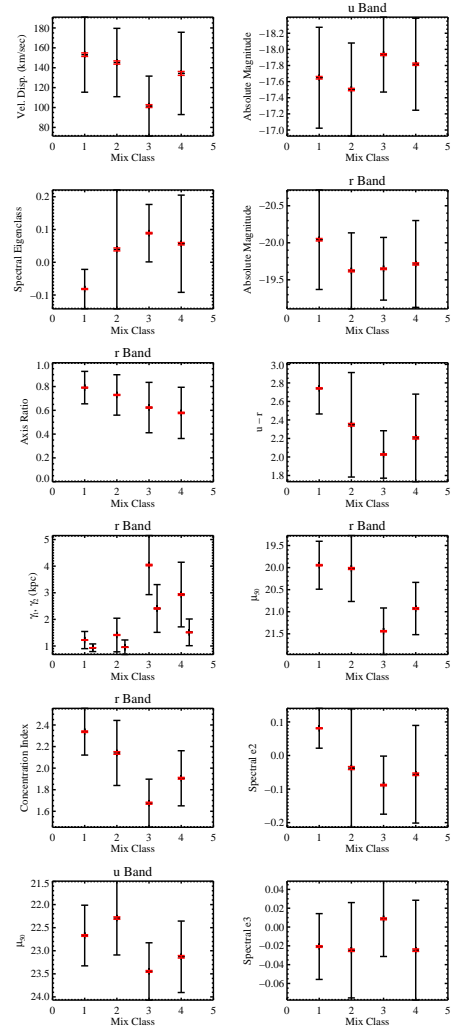


Fig. 15.— The average of several physical properties for each Mixture class. The larger error bars show the standard deviation in the distributions, and the shorter ones show the uncertainty in the mean. In the plot comparing γ_1 and γ_2 with M_k , γ_1 is the left (larger) data point and γ_2 is the right data point for each M_k .

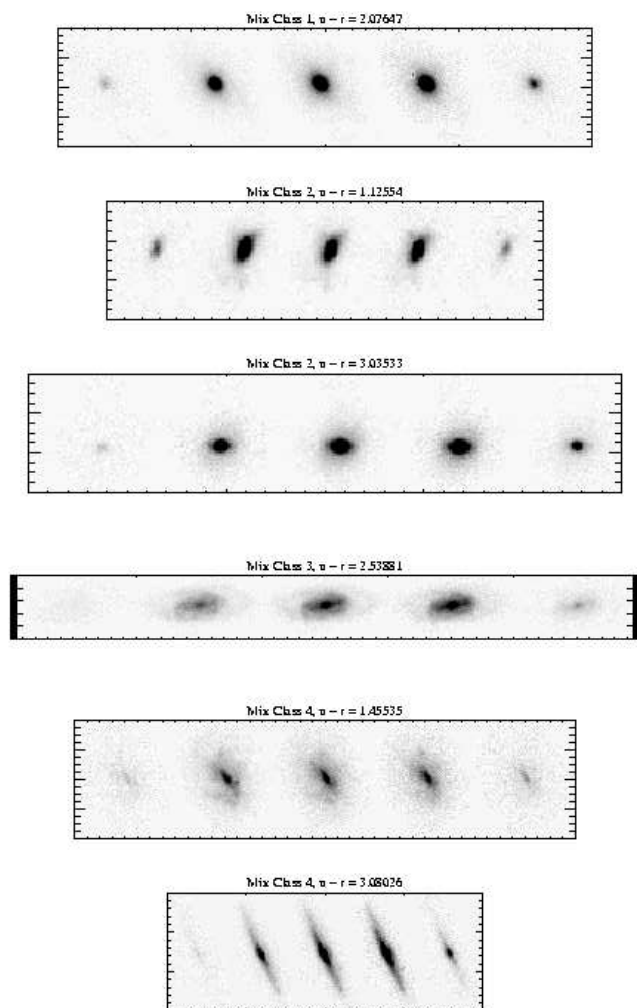


Fig. 16.— Selected galaxies from each mixture class with either a value of $u - r$ unexpected for that class, as the case for M_1 and M_3 , or a very ‘red’ or ‘blue’ value of $u - r$, as the case for M_2 and M_4 . We show these images for the purpose of comparing with a simple cut on $u - r$ color.

REFERENCES

- Abazajian, K. et al. 2003, *AJ*, 126, 2081
- Abraham, R. G., Tanvir, N. R., Santiago, B. X., Ellis, R. S., Glazebrook, K., & van den Bergh, S. 1996, *MNRAS*, 279, L47
- Abraham, R. G., van den Bergh, S., Glazebrook, K., Ellis, R. S., Santiago, B. X., Surma, P., & Griffiths, R. E. 1996, *ApJS*, 107, 1
- Abraham, R. G., van den Bergh, S., & Nair, P. 2003, *ApJ*, 588, 218
- Baldry, I. K., Glazebrook, K., Brinkmann, J., Ivezić, Z., Lupton, R.H., Nichol, R.C., & Szalay, A.S. 2003, *ApJ*, in press (astro-ph/0309710)
- Ball, N.M., Loveday, J., Fukugita, M., Nakamura, O., Okamura, S., Brinkmann, J., Brunner, R.J. 2003, submitted to *MNRAS*(astro-ph/0306390)
- Blanton, M.R., Lin, H., Lupton, R.H., Maley, F.M., Young, N., Zehavi, I., and Loveday, J. 2003, *AJ*, 125, 2276
- Block, D. L. & Wainscoat, R. J. 1991, *Nature*, 353, 48
- Block, D. L. & Puerari, I. 1999, *A&A*, 342, 627
- Colbert, J. W., Mulchaey, J. S., & Zabludoff, A. I. 2001, *AJ*, 121, 808
- Conselice, C. J. 2003, *ApJS*, 147, 1
- de Vaucouleurs, G., de Vaucouleurs, A., & Corwin, J. R. 1976, *Second reference catalogue of bright galaxies* (Austin: University of Texas Press)
- Doi, M., Fukugita, M., & Okamura, S. 1993, *MNRAS*, 264, 832
- Eisenstein, D.J., et al 2001, *AJ*, 122, 2267
- Eskridge, P. B. et al. 2002, *ApJS*, 143, 73
- Fischer, P., McKay, T.A., Sheldon, E. et al. 2000, *AJ*, 120, 1198
- Fukugita, M., Ichikawa, T., Gunn, J.E., Doi, M., Shimasaku, K., & Schneider, D.P. 1996, *AJ*, 111, 1748
- Gunn, J.E., Carr, M.A., Rockosi, C.M., Sekiguchi, M., et al. 1998, *AJ*, 116, 3040
- Hogg, D. W., Finkbeiner, D. P., Schlegel, D. J., & Gunn, J. E. 2001, *AJ*, 122, 2129
- Hubble, E.P. 1936, *The Realm of the Nebulae* (New Haven: Yale University Press)
- Jarrett, T. H. 2000, *PASP*, 112, 1008
- Lauger, S., Burgarella, D., & Buat, V. 2003, *Ap&SS*, 284, 969
- Lotz, J. M., Primack, J., & Madau, P. 2003, submitted to *AJ*(astro-ph/0311352)
- Kelly, B.C., McKay, T.A. 2003, in press at *AJ*(astro-ph/0307395)
- Moore, A.W. 1999, in *Advances in Neural Information Processing Systems 11*, ed. M. S. Kearns, S. A. Solla, & D. A. Cohn, (Cambridge : MIT Press)
- Morgan, W.W. 1958, *PASP*, 70, 364
- Nakamura, O., Fukugita, M., Yasuda, N., Loveday, J., Brinkmann, J., Schneider, D. P., Shimasaku, K., & SubbaRao, M. 2003, *AJ*, 125, 1682
- Odewahn, S.C. 1995, *PASP*, 107, 770
- Pier, J. R., Munn, J. A., Hindsley, R. B., Hennessy, G. S., Kent, S. M., Lupton, R. H., & Ivezić, Ž. 2003, *AJ*, 125, 1559
- Refregier, A. 2003, *MNRAS*, 338, 35
- Richards, G. et al. 2002, *AJ*, 123, 2945
- Smith, J. A. et al. 2002, *AJ*, 123, 2121
- Starck, J. L., Donoho, D. L., & Candès, E. J. 2003, *A&A*, 398, 785
- Stoughton, C.L. et al. 2002, *AJ*, 123, 485
- Strateva, I. et al. 2001, *AJ*, 122, 1861
- Strauss, M.A., et al 2002, *AJ*, 124, 1810
- Schweizer, F. 1976, *ApJS*, 31, 313
- van den Bergh, S., Cohen, J.G., & Crabbe, C. 2001, *AJ*, 122, 611
- Whyte, L. F., Abraham, R. G., Merrifield, M. R., Eskridge, P. B., Frogel, J. A., & Pogge, R. W. 2002, *MNRAS*, 336, 1281

Yip, C.W., Connolly, A.J. et. al. 2003, submitted

York, D. et al. 2000, AJ, 120, 1579

Zwicky, F. 1955, PASP, 67, 232